Chemical Science

ROYAL SOCIETY OF CHEMISTRY

EDGE ARTICLE

View Article Online
View Journal | View Issue



Cite this: *Chem. Sci.*, 2023, **14**, 8607

All publication charges for this article have been paid for by the Royal Society of Chemistry

# Curved graphene nanoribbons derived from tetrahydropyrene-based polyphenylenes *via* one-pot K-region oxidation and Scholl cyclization†

Sebastian Obermann, [a] Wenhao Zheng,[b] Jason Melidonie,[a] Steffen Böckmann, [c] Silvio Osella, [d] Nicolás Arisnabarreta, [e] L. Andrés Guerrero-León,[a] Felix Hennersdorf,[f] David Beljonne, [g] Jan J. Weigand, [f] Mischa Bonn, [b] Steven De Feyter, [e] Michael Ryan Hansen, [c] Hai I. Wang, [b] Ji Ma *[ah] and Xinliang Feng *[ah]

Precise synthesis of graphene nanoribbons (GNRs) is of great interest to chemists and materials scientists because of their unique opto-electronic properties and potential applications in carbon-based nanoelectronics and spintronics. In addition to the tunable edge structure and width, introducing curvature in GNRs is a powerful structural feature for their chemi-physical property modification. Here, we report an efficient solution synthesis of the first pyrene-based GNR (**PyGNR**) with curved geometry *via* one-pot K-region oxidation and Scholl cyclization of its corresponding well-soluble tetrahydropyrene-based polyphenylene precursor. The efficient $A_2B_2$-type Suzuki polymerization and subsequent Scholl reaction furnishes up to ~35 nm long curved GNRs bearing cove- and armchair-edges. The construction of model compound **1**, as a cutout of **PyGNR**, from a tetrahydropyrene-based oligophenylene precursor proves the concept and efficiency of the one-pot K-region oxidation and Scholl cyclization, which is clearly revealed by single crystal X-ray diffraction analysis. The structure and optical properties of **PyGNR** are investigated by Raman, FT-IR, solid-state NMR, STM and UV-Vis analysis with the support of DFT calculations. **PyGNR** exhibits a narrow optical bandgap of ~1.4 eV derived from a Tauc plot, qualifying as a low-bandgap GNR. Moreover, THz spectroscopy on **PyGNR** estimates its macroscopic charge mobility $\mu$ as ~3.6 $cm^2 V^{-1} s^{-1}$, outperforming several other curved GNRs reported *via* conventional Scholl reaction.

Received 2nd June 2023
Accepted 19th June 2023

DOI: 10.1039/d3sc02824k

rsc.li/chemical-science



## Introduction

Structurally well-defined graphene nanoribbons (GNRs) are constantly developing materials, amassing more and more attention due to their unique opto-electronic properties[1–3] and potential to be integrated into future nanoelectronics and spintronics.[3–9] The physicochemical properties of atomically precise GNRs highly depend on their edge structures and widths.[6,7,10–13] In the well-investigated armchair-edged GNRs (AGNR), three different families of ribbons can be distinguished as a function of carbon atoms along the ribbon width, exhibiting semiconducting properties.[6,14–21] On the other hand, zigzag-edged GNRs (ZGNR) possess edge states and metallic character, but could only be synthesized on surfaces to date, drastically limiting their applicability.[2,6,22–24] In stark contrast to largely uncontrolled top-down methods, the mentioned examples were achieved by bottom-up synthesis, an approach also rendering mixed edges possible. For instance, mixing armchair edge with zigzag edge can create intriguing physical phenomena, as recently exemplified by the topological quantum phase in GNRs.[7,25–27] Aside from the edge type, curvature (or non-

[a]*Center for Advancing Electronics Dresden (cfaed), Faculty of Chemistry and Food Chemistry, Technische Universität Dresden, D-01069 Dresden, Germany. E-mail: xinliang.feng@tu-dresden.de*

[b]*Max-Planck-Institute for Polymer Research, D-55128 Mainz, Germany*

[c]*Institute of Physical Chemistry, Westfälische Wilhelms-Universität (WWU) Münster, D-48149 Münster, Germany*

[d]*Chemical and Biological Systems Simulation Lab, Centre of New Technologies University of Warsaw, Banacha 2C, Warsaw 02-097, Poland*

[e]*Department of Chemistry, Division of Molecular Imaging and Photonics, KU Leuven, Celestijnenlaan 200F, 3001 Leuven, Belgium*

[f]*Chair of Inorganic Molecular Chemistry, Technische Universität Dresden, Dresden, Germany*

[g]*Laboratory for Chemistry of Novel Materials, Materials Research Institute, University of Mons, Mons 7000, Belgium*

[h]*Max Planck Institute of Microstructure Physics, Weinberg 2, 06120 Halle, Germany. E-mail: ji.ma@mpi-halle.mpg.de*

† Electronic supplementary information (ESI) available: Experimental details on synthetic procedures, NMR spectroscopy, HR MALDI-TOF mass, X-ray crystallography, GPC, THz-spectroscopy, solid-state NMR and DFT calculations (PDF). Crystal data for compound **1** and **10** (CIF). CCDC 2226715 and 2226716. For ESI and crystallographic data in CIF or other electronic format see DOI: https://doi.org/10.1039/d3sc02824k

planarity) is another powerful structural feature for tuning the properties of GNRs,[28,29] such as liquid-phase dispersibility and charge transport behavior.[30–32] A common synthetic pathway to achieve curvature in GNRs is to introduce the structural motif of small [*n*]helicene units on its periphery, such as [4]helicene or [5]helicene,[33–35] creating the cove edge[12,36–38] or fjord edge[39] respectively. For example, the regular incorporation of cove subunits by elimination of a single carbon atom along the opposite ZGNR edges can produce a series of curved GNRs with periodic cove-zigzag edge structure, providing GNRs with well-tunable band structures and effective masses (Fig. 1a).[11] In the context of this structural modification of ZGNRs towards cove-edge topologies, it raises the synthetic question if cove-edges can also be accessed from the parent design of AGNRs (Fig. 1b).

Pyrene (**2**) is one of the widely used building blocks in material science.[40] Its biphenyl-like structure with two double bond characteristics, called the K-region (Scheme 1), distinguishes pyrene from other polycyclic aromatic hydrocarbons (PAHs).[40,41] Moreover, its full-zigzag edge structure renders it a versatile motif for constructing highly conjugated π-systems with tailored edge topologies and functions. Although it is possible to functionalize pyrene on every position by various synthetic methods,[42–44] its incorporation into large PAHs (or nanographenes) *via* Scholl reaction of pyrene-based dendritic oligophenylene precursors is often unsuccessful due to its high reactivity and rich electron density.[45,46] Therefore, the expansion of pyrene-based precursors toward the synthesis of GNRs remains a synthetic challenge.

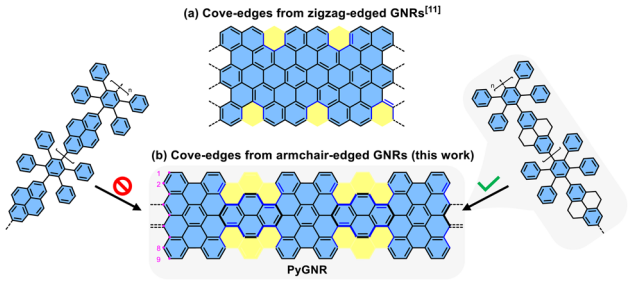


Fig. 1 (a) One example of curved GNRs with periodic cove-zigzag edges; (b) curved GNRs obtained by incorporation of cove units along the 9-AGNR edges, reported in this work.

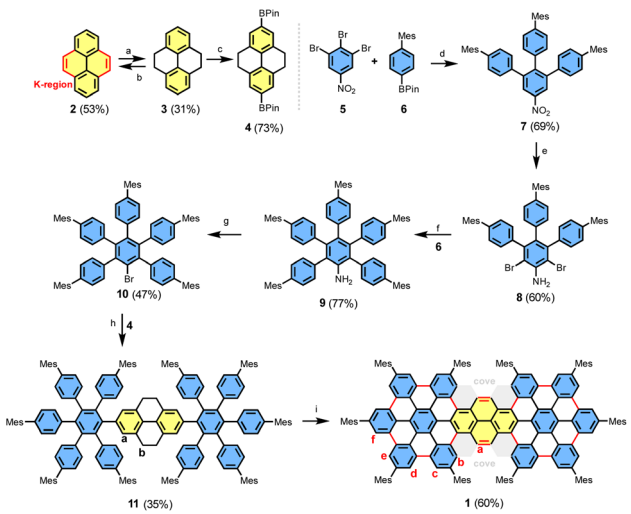


Scheme 1 Reoxidation of 4,5,9,10-tetrahydropyrene (**3**) and synthetic route to model compound **1**. Reagents and conditions: (a) (i) RANEY®-nickel, EtOAc, rt, 48 h, (ii) Pd/C (10%), EtOAc, $H_2$, 60 °C, 24 h; (b) $FeCl_3$ (10 eq.), $MeNO_2$, $CH_2Cl_2$, rt, 5 min; (c) $(BPin)_2$, 4,4′-di-*tert*-butyl-2,2′-bipyridine, $[Ir(OMe)(COD)]_2$, THF, 80 °C, overnight; (d) **5**, **6**, Pd(dppf)$Cl_2$·$CH_2Cl_2$, $K_3PO_4$, PhMe/$H_2O$, 115 °C, overnight; (e) (i) $SnCl_2$, EtOH/EtOAc, reflux, overnight, (ii) NBS, $CHCl_3$, rt, 10 min; (f) **6**, Pd(dppf)$Cl_2$, $K_3PO_4$, PhMe/$H_2O$, 115 °C, 48 h; (g) $CHBr_3$, isoamylnitrite, 100 °C, overnight; (h) $Pd(PPh_3)_4$, $K_2CO_3$, PhMe/$H_2O$, 115 °C, 48 h; (i) DDQ, $MeSO_3H$, $CH_2Cl_2$, rt, 30 min, then DDQ, TfOH, rt, 3 min.

Herein, we demonstrate an efficient solution synthesis of a novel curved pyrene-based GNR (**PyGNR**) bearing cove- and armchair-edges from the predesigned tetrahydropyrene-based polyphenylene precursor **P1**. It is worth mentioning that when trying to obtain **PyGNR** from pyrene-embedded polyphenylene directly (Fig. 1b), only short and insoluble oligomers could be obtained due to the poor solubility of the pyrene bearing polymers. To overcome this obstacle, the unsaturated polymer **P1** is first obtained by $A_2B_2$-Suzuki polymerization of 2,7-bis(4,4,5,5-tetramethyl-1,3,2-dioxaborolan-2-yl)-4,5,9,10-tetrahydro-pyrene (**4**) and alkyl-chain equipped tetraphenyl-substituted 1,4-diiodobenzene (**12**). Subsequently, one-pot oxidation of the tetrahydropyrene K-regions towards pyrene moieties together with the Scholl reaction, enables the desired formation of **PyGNR**. The resultant **PyGNR** reaches a length of up to ~35 nm according to the gel-permeation chromatography (GPC) analysis of **P1**. As a cutout of **PyGNR**, model compound **1** was successfully synthesized to evaluate the efficiency and feasibility of the one-pot cyclodehydrogenation process. The structure and optical properties of **PyGNR** were well investigated by solid-state NMR, FT-IR, Raman, STM imaging and UV-Vis spectroscopy. Due to the unique edge structure, a narrow optical bandgap of ~1.4 eV was determined by a Tauc-plot (ESI Fig. S2†), slightly below the value of 1.75 eV predicted by DFT. Furthermore, time-resolved terahertz spectroscopy reveals a macroscopic charge mobility of ~3.6 $cm^2\ V^{-1}\ s^{-1}$, outperforming several other examples[37,39] of curved GNRs obtained by conventional Scholl reactions.

## Results and discussion

### Synthesis of model compound 1

The synthesis of model compound **1** is illustrated in Scheme 1. Considering the solubility issue of **1**, mesitylene side groups were installed instead of the more common *tert*-butyl groups. First, 4,5,9,10-tetrahydropyrene (**3**) was obtained from the commercially available pyrene (**2**) after desulfurization with RANEY®-nickel and hydrogenation under pressure in the presence of Pd/C among over-hydrogenated products in 31% yield (Scheme 1). Then, iridium-catalyzed borylation[42] was used to furnish compound **4** in 73% yield. Slightly modifying the synthesis route of Lungerich *et al.*[47] allowed us to synthesize compound **10** starting from 1,2,3-tribromo-5-nitrobenzene (**5**, see ESI†). A Suzuki coupling reaction between **5** and **6** afforded compound **7** in 69% yield, followed by a two-step sequence of

reduction and bromination to furnish compound **8** in 60% yield. Another Suzuki coupling of **8** and **6** gave compound **9** in 77% yield. In a Sandmeyer-type reaction, aniline **9** was brominated to compound **10** with a yield of 47%. Finally, building blocks **4** and **10** were cross-coupled by the Suzuki reaction, providing the oligophenylene precursor **11** in a low yield of 35% due to the steric hindrance of the inner mesitylene units in **11**. For the cyclodehydrogenation of **11**, we initially examined the classic Scholl conditions by use of $FeCl_3$ or triflic acid with DDQ in $CH_2Cl_2$, but failed to obtain a defined product (ESI Chapter 1.2.12†). We then turned to a milder approach using methylsulfonic acid, and DDQ, which furnished a time-stable MALDI-TOF signal 12 proton masses above the desired signal, indicating a partially closed intermediate (ESI Fig. S32†).

After adding the stronger triflic acid to the reaction mixture, the bright red compound **1** was obtained in 60% yield after only three minutes of additional reaction time.

The chemical identity of **1** was confirmed by high-resolution mass spectroscopy and NMR spectroscopy, whose key changes for compounds **11** and **1** are illustrated in Fig. 2, respectively. The MALDI-TOF spectra show a mass difference of 28 proton masses. This implies that in addition to the cyclodehydrogenation of 24 protons, 4 additional hydrogens were removed from the tetrahydropyrene moiety to reestablish the pyrene K-region. In addition to the reduction of NMR signals in the case of compound **1**, the total amount of protons in the aliphatic region was reduced from 98 to 90 (ESI Fig. S19–S21†), further confirming the successful conversion of the tetrahydropyrene moieties. The anti π–π-stacking properties of the mesitylene side groups enabled NMR spectroscopy of **1** with a sufficient resolution to assign the protons using two-dimensional COSY- and NOESY-NMR spectroscopy (ESI Fig. S22 and S23†). Furthermore, a shift in the downfield due to the aromatic ring currents was observed, especially for the protons a and b (proton labels seen in Scheme 1), resulting from their location on the cove edge.

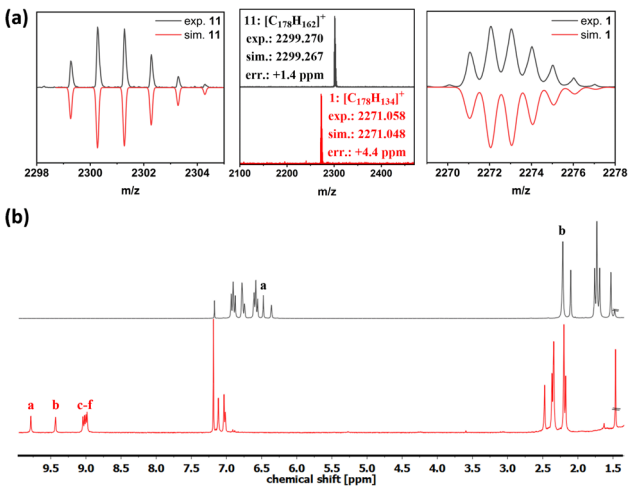


Fig. 2 (a) MALDI-TOF-MS of compounds **11** and **1**. (b) $^1$H-NMR spectra of compound **11** (top) and compound **1** (bottom), recorded in $CDCl_3$ at 300 MHz (proton labels see Scheme 1).

## Crystallographic analysis of compounds 11 and 1

Sufficiently large crystals for X-ray crystallographic analysis were obtained for **11** and **1**, respectively (Fig. 3). In the case of **11**, a suitable crystal for single crystal X-ray diffraction analysis (SCXRD) was grown from **11** dissolved in $CH_2Cl_2$ by slow evaporation of the solvent. SCXRD reveals an unconjugated phenylic structure combined with twisted $sp^3$-bonds of the central tetrahydropyrene unit. The $sp^3$-carbon single bonds are revealed by the bond lengths of 1.57 Å and 1.58 Å, respectively. Compound **11** crystallizes in the triclinic space group *P*1. In the case of **1**, a single crystal was obtained by slow diffusion of methanol in its $CS_2$-solution. The SCXRD analysis reveals **1** as a curved π-conjugated molecule featuring four [4]helicene subunits. The hexa-*peri*-hexabenzocoronene (HBC) units have been fully fused and share a pyrene unit in the center, revealing the successful conversion of the tetrahydropyrene moieties back to a fully $sp^2$-hybridized pyrene core and supporting the proposed one-pot K-region oxidation and Scholl cyclization. The cove edges between the pyrene K-region and the HBC moieties possess an average torsion angle of 21°, resulting in curvature of the molecule. In contrast to compound **11**, compound **1** crystallizes in the monoclinic space group $P2_1/c$. The bond lengths in the K-regions of compound **1** are significantly shorter, about 1.35 Å (1.337 Å and 1.361 Å, respectively), matching with the value for pyrene (**2**) reported by the literature and indicating double bond character.[48] In the solid packing, the crystal layers of **1** are slightly slipped with the π-surfaces facing towards each other, forming π–π-stacks (Fig. 3c).

## Synthesis of PyGNR

After confirming the model reaction formed the desired compound **1**, we further extended the synthesis towards **PyGNR** based on tetrahydropyrene monomer **4**. Early attempts of this

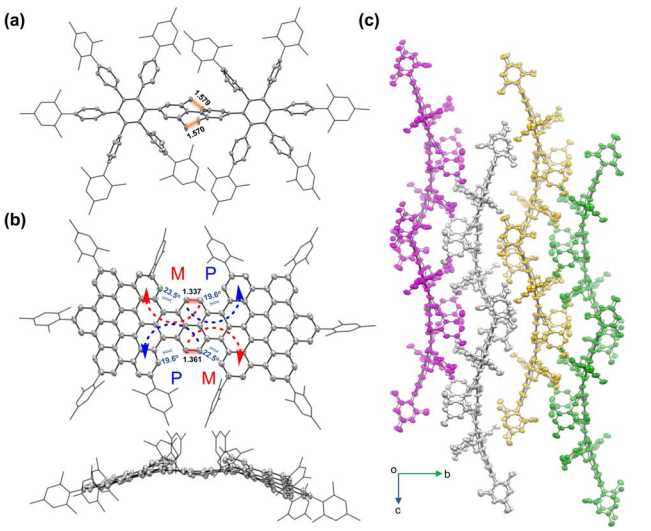


Fig. 3 X-ray crystallographic structure (ORTEP drawing at the 50% probability level) of (a) **11** and (b) **1** (top and side view). (c) Crystal-packing of **1**. Hydrogen atoms and solvent molecules have been omitted for clarity.

$A_2B_2$ Suzuki polymerization with 2,7-diborylated pyrene gave only oligomers according to linear mode MALDI-TOF MS measurements, which remained insoluble and, therefore, unavailable for further solution processing (ESI Fig. S34†). When these oligomers were exposed to Scholl-reaction conditions as a suspension, partial cyclization and decomposition were observed. In consequence, the 4,5,9,10-tetrahydropyrene containing polymer **P1** (Scheme 2) was designed. The monomer **12**,[15] substituted with 3,7-dimethyloctyl chains, was chosen as the coupling partner for the diborylated pyrene derivative **4** to increase the processibility of the GNR later. In contrast to pyrene (**2**), when switching to the tetrahydropyrene derivative **4**, soluble polymers were obtained when refluxing the monomers, $Pd(PPh_3)_4$, $K_2CO_3$ in toluene and $H_2O$ for 48 hours. Linear mode MALDI-TOF MS of the crude material revealed groups of signals up to $m/z \sim 10\,000$, spaced by the repetition unit of 1145 g mol$^{-1}$ (ESI Fig. S33†). After washing with HCl/MeOH, filtration and subsequent dissolution and filtration in chloroform, the crude polymer **P1** was obtained after removing the chloroform *in vacuo*. **P1** was then divided into 4 fractions by recycling GPC and further analyzed by analytical GPC against polystyrene standards. Our analysis reveals an averaged molar mass of $M_n \sim 24\,000$ Da and a narrow polydispersity index (PDI) of 1.2 for the heaviest (10 wt%) crude polymers (ESI Fig. S36–S38†), significantly enhancing the molecular weight compared to other GNRs reported *via* the Suzuki polymerization method.[15,39] The protons could be assigned to their positions in **P1** by $^1$H-NMR spectroscopy (ESI Fig. S30†). Due to **P1**'s excellent solubility, even $^{13}$C spectra could be recorded effortlessly (ESI Fig. S31†). Finally, the Scholl reaction of the first fraction of **P1** with $FeCl_3$ (7 equiv./H) as the Lewis acid and oxidant in $CH_2Cl_2$ for 7 days yielded the **PyGNR**. The resultant **PyGNR** possesses combined cove and armchair edges with an estimated average length of ~35 nm based on the $M_n$ of the corresponding **P1**.

### Structural characterizations of PyGNR

The structures of precursor **P1** and **PyGNR** were then characterized by a combination of solid-state $^1$H and $^{13}C\{^1H\}$ MAS NMR ($^1$H decoupled $^{13}$C magic angle spinning NMR) at a high spinning speed of 62.5 kHz (Fig. 4a and b), FT-IR and Raman (Fig. 4c and d). While the precursor **P1** shows well-defined signals in the $^1$H MAS NMR spectrum (Fig. 4a) for both the aromatic and aliphatic protons centered around 0.9 ppm and 6.6 ppm, respectively, broader lines are observed for **PyGNR** along with a downfield shift of the aromatic protons to 8.9 ppm. This can be attributed to a more rigid structure and extended π-conjugation of **PyGNR** compared to **P1**. Deconvolution of the quantitative $^1$H MAS NMR spectra shows a lower relative content of aromatic protons in **PyGNR** compared to **P1** as a result of the graphitization and matches the expected relative intensities within the expected error margins. The graphitization process can also be confirmed by the $^{13}C\{^1H\}$ MAS NMR spectra that were acquired with a short recycle delay of 3.5 s (Fig. 4b). Under the chosen experimental conditions, the $^{13}$C signal of the side chains only shows low intensity. In addition, the structural evolution from **P1** to **PyGNR** is also supported by 2D solid-state NMR experiments (see ESI Chapter 9†).

The FT-IR spectra of **P1** (Fig. 4c) exhibit typical vibrational modes for its structural elements. A more detailed discussion can be found in Chapter 10 of the ESI.† To assist in the identification of the corresponding vibrations, DFT calculations on the HSE/6-31G(d) level of theory were performed. The peak at 885 cm$^{-1}$, which was identified as the SOLO-mode (CH-wagging of an aromatic proton without adjacent protons, orange)[49] of the tetrahydropyrene moiety, confirms once more the presence of unsaturated bonds in **P1**. The FT-IR spectrum of **PyGNR** was then compared to **P1**. The abundant aromatic CH-stretchings in the range of 3020–3060 cm$^{-1}$ were diminished in the graphitized ribbon due to the cyclodehydrogenation. The CH-stretchings from the aliphatic side chains from 2750 to 3000 cm$^{-1}$ were retained. Further, characteristic vibrations were investigated in the fingerprint region and identified by comparison to the HSE/6-31G(d) prediction. First, the SOLO-modes can be found around 882 cm$^{-1}$ (pink), a further indication of successful graphitization. Interestingly, **PyGNR**s CH-wagging of the cove SOLO-mode and pyrene DUO moieties

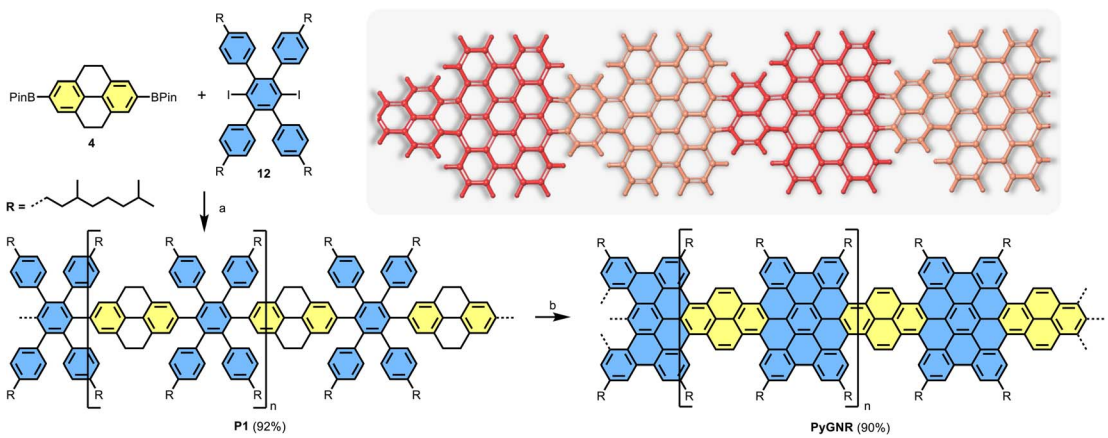


Scheme 2 Synthetic route to **PyGNR**. Reagents and conditions: (a) **4** (stoichiometric), **12**, $Pd(PPh_3)_4$, $K_2CO_3$, Aliquat 336, PhMe/$H_2O$, 110 °C, 48 h; (b) $FeCl_3$, $MeNO_2$, $CH_2Cl_2$, rt, 7 d. Inset is the optimized geometry of **PyGNR**, aliphatic side chains omitted for clarity.

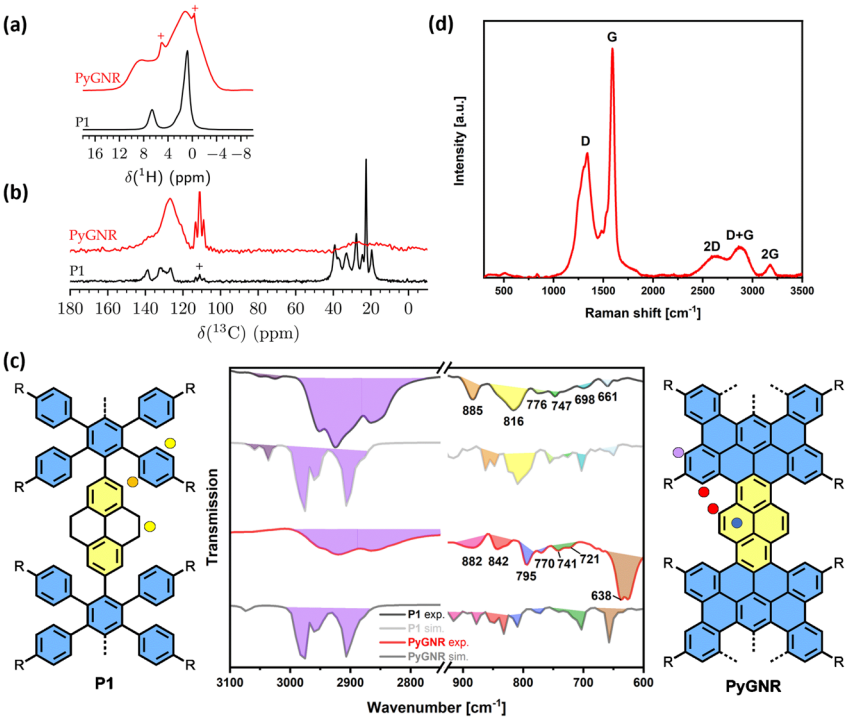


Fig. 4 (a) Quantitative $^{1}$H MAS NMR spectra of **P1** and **PyGNR** with 64 s recycle delay. Signals of remaining solvent are marked with +; (b) $^{13}$C{1H} MAS NMR spectra with a short recycle delay of 3.5 s and 25 kHz of low-power CW decoupling. The signal of PTFE spacer material is marked with +. All spectra were acquired at a static field of 11.74 T and a spinning frequency of 62.5 kHz. (c) Measured and calculated (at the DFT HSE/6-31G(d) level) FT-IR spectra of **P1** and **PyGNR**. In the fingerprint region (900–600 cm$^{-1}$), the calculated IR intensity was scaled by a factor 10; (d) Raman spectra of **PyGNR**, recorded at 514 nm.

(CH-wagging of two adjacent aromatic protons) can be found in a joint vibration mode around 840 cm$^{-1}$ (red), demonstrating the successful conversion of the tetrahydro-moieties into pyrene K-regions. This claim is further supported by the ring vibrations of the pyrene K-region, which can be attributed to the newly emerged signals around 790–770 cm$^{-1}$ (blue), absent in **P1**. Last, the broad signal at 640 cm$^{-1}$ (brown) provides another strong indication of successful graphitization, as the DFT-prediction assigns these modes as in plane aromatic CC-scaffold vibrations. The Raman spectrum of **PyGNR** (Fig. 4d) shows two strong D and G bands at ~1340 and ~1590 cm$^{-1}$. Furthermore, double resonance peaks can be found at ~2605, ~2880 and ~3170 cm$^{-1}$, which can be assigned as the 2D, D + G and 2G bands. The peak positions are in line with other bottom-up solution-synthesized GNRs reported in the literature.[13,21,37] As expected from the low twist in the cove regions observed from the crystal structure of compound **1** (21°), **PyGNR** shows only mediocre dispersibility and processability in polar organic solvents. However, imaging techniques such as STM vastly favor planar structures and usually fail to yield results for strongly curved geometries. Fig. 5 shows the results obtained by the STM characterization of **PyGNR** at the HOPG/heptanoic acid interface. Large scale (Fig. 5a) and high resolution (Fig. 5b) STM images show the presence of a clear stripe patterned structure observed in isolated areas of the HOPG surface. Line profile analysis performed in graphite calibrated STM images (Fig. 5c) confirms the presence of parallel rows comprising a periodicity of 3.3 (±0.2) nm which matches the expected periodicity from molecular modelling (Fig. 5d). This distance indicates that **PyGNR** is adsorbed without alkyl chain interdigitation, but instead, next to one another[50] as depicted in Fig. 5d. The stability obtained during the STM measurements suggests high on-surface adsorption energies due to strong vdW-interactions between the **PyGNR** core and the graphitic substrate. This

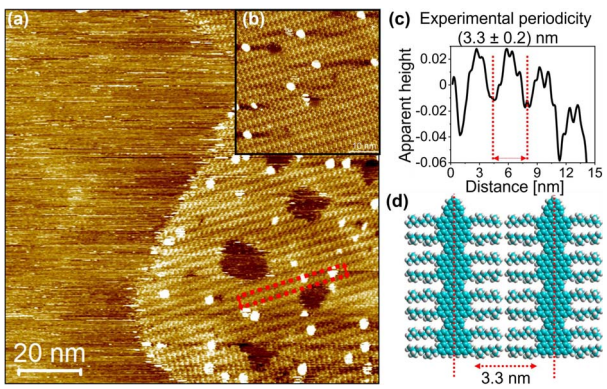


Fig. 5 Large scale (a) and high resolution (b) STM images of **PyGNR** self-assembled at the heptanoic acid/HOPG interface; (c) graphite-calibrated representative line-profile measured along the red arrow direction in STM image of panel (a); (d) molecular model of **PyGNR** showing packing without alkyl chain interdigitation. $U_{bias} = -0.4$ V and $I_{set} = 0.05$ nA.

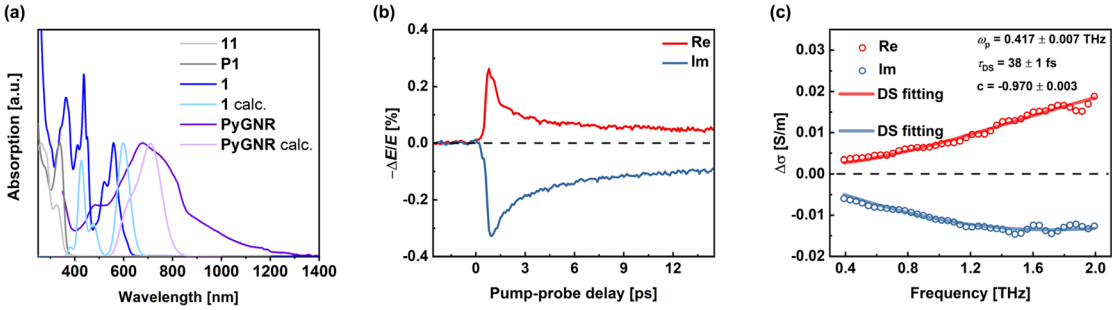


Fig. 6 (a) Absorption spectra of **1**, **11**, **P1** ($CHCl_3$), and **PyGNR** (NMP) as well as DFT-predicted **1** and **PyGNR**; (b) time-resolved terahertz photoconductivity of **PyGNR** following photoexcitation. The absorbed photon fluence is ~1 mJ $cm^{-2}$. (c) The frequency-resolved THz complex conductivity measured ~1.2 ps after photoexcitation. The solid lines are fits to the Drude–Smith model.

allowed the acquisition of multiple STM images (see ESI Fig. S51†).

In contrast, the low twist of **PyGNR** seems to be sufficient to resolve the π–π-interactions observed in planar GNRs,[15] as additional investigations by TEM, SEM and powder XRD revealed an amorphous structure of the material (see ESI Chapters 11–13†). Subsequent to SEM imaging, EDX confirmed the complete removal of residual iron ions (see ESI Chapter 11†).

### Optical property and THz spectroscopy study of PyGNR

The UV-Vis absorption spectra were recorded in $CHCl_3$ solutions. An NMP dispersion of **PyGNR** that was allowed to settle overnight was used (Fig. 6a). Due to its lack of conjugation, polymer **P1** (dark grey) possesses only high energy absorption bands starting with a first peak at 338 nm, which agrees well with the polymer fragment **11** (light gray), exhibiting peaks at similar wavelengths (326 nm and 267 nm). Significantly red-shifted to 559 nm due to its full conjugation, the first absorption of **1** (blue) can be found. Two distinct absorption peaks of **1** are visible at 437 nm and 367 nm.

Compared to its short fragment **1**, the absorption spectrum of **PyGNR** (purple) is further red-shifted and displays an absorption peak with a maximum at ~680 nm as well as a shoulder at 485 nm, showing strong proof for graphitization compared to the high energy absorptions of **P1**. The optical bandgap was determined as 1.4 eV by a Tauc-plot (ESI Fig. S2†), qualifying as a low bandgap GNR. The experimental result is in good agreement with the DFT-prediction of 1.75 eV. In addition, the simulated TD-DFT curves for **1** (light blue) and **PyGNR** (light purple) match well with the experimental spectra.

To investigate the charge transport properties of **PyGNR**, we conducted optical pump-THz probe (OPTP) spectroscopy measurements (see the Experimental details in the ESI Chapter 8†).[51,52] Fig. 6b shows the time-resolved complex photoconductivity of **PyGNR** dispersed in 1,2,4-trichlorobenzene, following above-gap optical excitation (here, 1.55 eV laser pulses). The rapid sub-picosecond rise of the real photoconductivity indicates charge carrier generation, and the following rapid decay can be assigned to the carrier trapping and/or the formation of bound electron–hole states (*i.e.*, excitons) due to the strong quantum confinement and the reduced dielectric screening effect.[52,53] The exciton formation is featured by a large imaginary conductivity and a small real conductivity at the later time scale. To further study the free charge carriers' transport properties, we measured the conductivity spectrum around the peak photoconductivity (~1.2 ps after photoexcitation), as shown in Fig. 6c (for Experimental details, see ESI Chapter 8†). The phenomenological Drude–Smith (DS) model was applied to describe the frequency-resolved complex conductivity (for details, see ESI†).[54,55] The DS model considers the charge scattering occurring *via* preferential backscattering due to conjugation or structural deformation in materials. A parameter $c$ is introduced to characterize the backscattering probability, ranging from 0 (isotropic scattering) to −1 (100% backscattering). From the results, we obtained an effective charge scattering time $\tau = 38 \pm 1$ fs and $c = -0.970 \pm 0.003$. Furthermore, by considering a reduced charge carrier effective mass $m^* = 0.55m_0$ from DFT (considering contributions from both electrons and holes; see the ESI† for details), we estimate the macroscopic charge mobility $\left(\mu = \frac{e\tau}{m^*}(1+c)\right)$ to be ~3.6 $cm^2$ $V^{-1}$ $s^{-1}$, outperforming similar examples of curved GNRs in the recent literature, such as hybrid cove- and gulf-edged GNRs,[37] and a 9AGNR based fjord-edged GNR.[39]

## Conclusion

In summary, we demonstrate the efficient synthesis of the first curved pyrene-based GNR (**PyGNR**) by introducing cove units along 9-AGNR edges. The synthetic strategy to obtain **PyGNR** was carried out in a previously unreported strategy, regenerating the K-regions of the pyrene moieties in one step during the cyclodehydrogenation of a well-soluble unsaturated polyphenylene precursor **P1**. Proving the structural concept of the ribbon and the proposed one-pot oxidation, model compound **1** was also synthesized. The obtained **PyGNR** was fully characterized by solid-state NMR, FT-IR, Raman, STM and UV-Vis spectroscopy, also supported by the DFT spectra simulations. THz study of **PyGNR** revealed a macroscopic charge mobility of ~3.6 $cm^2$ $V^{-1}$ $s^{-1}$, outperforming similar GNRs reported by conventional Scholl-cyclizations.[37,39] Furthermore, **PyGNR** is the first GNR with accessible pyrene K-regions, rendering further functionalization, *e.g.*, by oxidation to diketones, possible.[43]

Strategic use of tetrahydro-derivatives demonstrates the feasibility of obtaining novel GNRs in one step from $sp^3$-C containing polymer precursors and opens up possibilities for other GNRs suffering from polymer solubility issues or dehydrogenation problems.

## Data availability

Experimental and computational data can be found in the ESI.† The cif-files of the crystal structures can be found alongside the ESI.†

## Author contributions

J. Ma and X. Feng supervised the project. S. Obermann, J. Melidonie and L. A. Guerrero-León synthesized and characterized the compounds. W. Zheng, M. Bonn and H. I. Wang measured and interpreted the THz measurements. S. Böckmann and M. R. Hansen measured and interpreted the solid-state NMR. S. Osella and D. Beljonne performed the DFT calculations. N. Arisnabarreta and S. De Feyter carried out and analyzed the solid-liquid STM imaging. F. Hennersdorf and J. J. Weig and measured and refined the single crystal structures. S. Obermann, J. Ma and X. Feng co-wrote the paper with contributions from all co-authors.

## Conflicts of interest

The authors declare no conflict of interest.

## Acknowledgements

This research was financially supported by the EU Graphene Flagship (Graphene Core 3, 881603), ERC Consolidator Grant (T2DCP, 819698), H2020-MSCA-ITN (ULTIMATE, No. 813036), the Center for Advancing Electronics Dresden (cfaed), H2020-EU.1.2.2.-FET Proactive Grant (LIGHT-CAP, 101017821), the DFG-SNSF Joint Switzerland-German Research Project (Enhan-Topo, No. 429265950) and the Research Foundation–Flanders (FWO) (grant G.0A41.20N, 12ZS623N), KU Leuven Internal Funds (grants C14/18/06 and C14/19/079). The authors gratefully acknowledge the GWK support for funding this project by providing computing time through the Center for Information Services and HPC (ZIH) at TU Dresden. The computational resources in Mons are supported by the FNRS "Consortium des Equipments de Calcul Intensif–CECI" program Grant No. 2.5020.11 and by the Walloon Region (ZENOBE Tier-1 supercomputer, under grant 1117545). D. B. is a research director at Belgian F.R.S./FNRS. We also thank the Polish National Science Centre for funding (grant no. UMO-2020-39-I-ST4-01446). The computation was carried out with the support of the Interdisciplinary Center for Mathematical and Computational Modeling at the University of Warsaw (ICM UW) under grants no. (G83-28 and GB80-24). The authors also express their gratitude to Markus Göbel for the Raman measurement, Frank Drescher for the ESI-measurements, Enrique Caldera Cruz for the analytical GPC measurements and Tobias Nickel for the MALDI-TOF measurements. N. A. acknowledges K. S. Mali for fruitful discussions.

## References

1 J. Cai, C. A. Pignedoli, L. Talirz, P. Ruffieux, H. Söde, L. Liang, V. Meunier, R. Berger, R. Li, X. Feng, K. Müllen and R. Fasel, *Nat. Nanotechnol.*, 2014, **9**, 896–900.
2 P. Ruffieux, S. Wang, B. Yang, C. Sanchez-Sanchez, J. Liu, T. Dienel, L. Talirz, P. Shinde, C. A. Pignedoli, D. Passerone, T. Dumslaff, X. Feng, K. Müllen and R. Fasel, *Nature*, 2016, **531**, 489–492.
3 W. Niu, J. Ma, P. Soltani, W. Zheng, F. Liu, A. A. Popov, J. J. Weigand, H. Komber, E. Poliani, C. Casiraghi, J. Droste, M. R. Hansen, S. Osella, D. Beljonne, M. Bonn, H. I. Wang, X. Feng, J. Liu and Y. Mai, *J. Am. Chem. Soc.*, 2020, **142**, 18293–18298.
4 X. Li, X. Wang, L. Zhang, S. Lee and H. Dai, *Science*, 2008, **319**, 1229–1231.
5 V. Saraswat, R. M. Jacobberger and M. S. Arnold, *ACS Nano*, 2021, **15**, 3674–3708.
6 O. v. Yazyev, *Acc. Chem. Res.*, 2013, **46**, 2319–2328.
7 D. J. Rizzo, G. Veber, T. Cao, C. Bronner, T. Chen, F. Zhao, H. Rodriguez, S. G. Louie, M. F. Crommie and F. R. Fischer, *Nature*, 2018, **560**, 204–208.
8 Y. Huang, W. T. Dou, F. Xu, H. B. Ru, Q. Gong, D. Wu, D. Yan, H. Tian, X. P. He, Y. Mai and X. Feng, *Angew. Chem., Int. Ed.*, 2018, **57**, 3366–3371.
9 A. Narita, X. Y. Wang, X. Feng and K. Müllen, *Chem. Soc. Rev.*, 2015, **44**, 6616–6643.
10 Y. F. Zhang, Y. Zhang, G. Li, J. Lu, Y. Que, H. Chen, R. Berger, X. Feng, K. Müllen, X. Lin, Y. Y. Zhang, S. Du, S. T. Pantelides and H. J. Gao, *Nano Res.*, 2017, **10**, 3377–3384.
11 X. Wang, J. Ma, W. Zheng, S. Osella, N. Arisnabarreta, J. Droste, G. Serra, O. Ivasenko, A. Lucotti, D. Beljonne, M. Bonn, X. Liu, M. R. Hansen, M. Tommasini, S. De Feyter, J. Liu, H. I. Wang and X. Feng, *J. Am. Chem. Soc.*, 2022, **144**, 228–235.
12 J. Liu, B. W. Li, Y. Z. Tan, A. Giannakopoulos, C. Sanchez-Sanchez, D. Beljonne, P. Ruffieux, R. Fasel, X. Feng and K. Müllen, *J. Am. Chem. Soc.*, 2015, **137**, 6097–6103.
13 M. G. Schwab, A. Narita, Y. Hernandez, T. Balandina, K. S. Mali, S. de Feyter, X. Feng and K. Müllen, *J. Am. Chem. Soc.*, 2012, **134**, 18169–18172.
14 W. Yang, A. Lucotti, M. Tommasini and W. A. Chalifoux, *J. Am. Chem. Soc.*, 2016, **138**, 9137–9144.
15 X. Yang, X. Dou, A. Rouhanipour, L. Zhi, H. J. Räder and K. Müllen, *J. Am. Chem. Soc.*, 2008, **130**, 4216–4217.
16 J. Cai, P. Ruffieux, R. Jaafar, M. Bieri, T. Braun, S. Blankenburg, M. Muoth, A. P. Seitsonen, M. Saleh, X. Feng, K. Müllen and R. Fasel, *Nature*, 2010, **466**, 470–473.
17 R. S. Jordan, Y. L. Li, C. W. Lin, R. D. McCurdy, J. B. Lin, J. L. Brosmer, K. L. Marsh, S. I. Khan, K. N. Houk, R. B. Kaner and Y. Rubin, *J. Am. Chem. Soc.*, 2017, **139**, 15878–15890.
18 L. Talirz, H. Söde, T. Dumslaff, S. Wang, J. R. Sanchez-Valencia, J. Liu, P. Shinde, C. A. Pignedoli, L. Liang,

V. Meunier, N. C. Plumb, M. Shi, X. Feng, A. Narita, K. Müllen, R. Fasel and P. Ruffieux, *ACS Nano*, 2017, **11**, 1380–1388.
19 K. Sun, P. Ji, J. Zhang, J. Wang, X. Li, X. Xu, H. Zhang and L. Chi, *Small*, 2019, **15**, 1804526.
20 K. Y. Yoon and G. Dong, *Mater. Chem. Front.*, 2020, **4**, 29–45.
21 G. Li, K. Y. Yoon, X. Zhong, J. Wang, R. Zhang, J. R. Guest, J. Wen, X. Y. Zhu and G. Dong, *Nat. Commun.*, 2018, **9**, 1687.
22 S. Wang, L. Talirz, C. A. Pignedoli, X. Feng, K. Müllen, R. Fasel and P. Ruffieux, *Nat. Commun.*, 2016, **7**, 11507.
23 P. P. Shinde, J. Liu, T. Dienel, O. Gröning, T. Dumslaff, M. Mühlinghaus, A. Narita, K. Müllen, C. A. Pignedoli, R. Fasel, P. Ruffieux and D. Passerone, *Carbon*, 2021, **175**, 50–59.
24 P. P. Shinde, O. Gröning, S. Wang, P. Ruffieux, C. A. Pignedoli, R. Fasel and D. Passerone, *Carbon*, 2017, **124**, 123–132.
25 Y. L. Lee, F. Zhao, T. Cao, J. Ihm and S. G. Louie, *Nano Lett.*, 2018, **18**, 7247–7253.
26 T. Cao, F. Zhao and S. G. Louie, *Phys. Rev. Lett.*, 2017, **119**, 076401.
27 O. Gröning, S. Wang, X. Yao, C. A. Pignedoli, G. Borin Barin, C. Daniels, A. Cupo, V. Meunier, X. Feng, A. Narita, K. Müllen, P. Ruffieux and R. Fasel, *Nature*, 2018, **560**, 209–213.
28 Y. Hu, P. Xie, M. de Corato, A. Ruini, S. Zhao, F. Meggendorfer, L. A. Straasø, L. Rondin, P. Simon, J. Li, J. J. Finley, M. R. Hansen, J. S. Lauret, E. Molinari, X. Feng, J. v. Barth, C. A. Palma, D. Prezzi, K. Müllen and A. Narita, *J. Am. Chem. Soc.*, 2018, **140**, 7803–7809.
29 W. Niu, J. Ma and X. Feng, *Acc. Chem. Res.*, 2022, **55**, 3322–3333.
30 N. J. Schuster, L. A. Joyce, D. W. Paley, F. Ng, M. L. Steigerwald and C. Nuckolls, *J. Am. Chem. Soc.*, 2020, **142**, 7066–7074.
31 M. Ball, Y. Zhong, Y. Wu, C. Schenck, F. Ng, M. Steigerwald, S. Xiao and C. Nuckolls, *Acc. Chem. Res.*, 2015, **48**, 267–276.
32 I. Ivanov, Y. Hu, S. Osella, U. Beser, H. I. Wang, D. Beljonne, A. Narita, K. Müllen, D. Turchinovich and M. Bonn, *J. Am. Chem. Soc.*, 2017, **139**, 7982–7988.
33 Y. Shen and C. F. Chen, *Chem. Rev.*, 2012, **112**, 1463–1535.
34 M. Gingras, G. Félix and R. Peresutti, *Chem. Soc. Rev.*, 2013, **42**, 1007–1050.
35 C. Li, Y. Yang and Q. Miao, *Chem.–Asian J.*, 2018, **13**, 884–894.
36 T. J. Sisto, Y. Zhong, B. Zhang, M. T. Trinh, K. Miyata, X. Zhong, X. Y. Zhu, M. L. Steigerwald, F. Ng and C. Nuckolls, *J. Am. Chem. Soc.*, 2017, **139**, 5648–5651.
37 L. Yang, J. Ma, W. Zheng, S. Osella, J. Droste, H. Komber, K. Liu, S. Böckmann, D. Beljonne, M. R. Hansen, M. Bonn, H. I. Wang, J. Liu and X. Feng, *Adv. Sci.*, 2022, **9**, 2200708.
38 Y. Zhong, B. Kumar, S. Oh, M. T. Trinh, Y. Wu, K. Elbert, P. Li, X. Zhu, S. Xiao, F. Ng, M. L. Steigerwald and C. Nuckolls, *J. Am. Chem. Soc.*, 2014, **136**, 8122–8130.
39 X. Yao, W. Zheng, S. Osella, Z. Qiu, S. Fu, D. Schollmeyer, B. Müller, D. Beljonne, M. Bonn, H. I. Wang, K. Müllen and A. Narita, *J. Am. Chem. Soc.*, 2021, **143**, 5654–5658.
40 T. M. Figueira-Duarte and K. Müllen, *Chem. Rev.*, 2011, **111**, 7260–7314.
41 S. Sasaki, S. Suzuki, K. Igawa, K. Morokuma and G. Konishi, *J. Org. Chem.*, 2017, **82**, 6865–6873.
42 L. Ji, K. Fucke, S. K. Bose and T. B. Marder, *J. Org. Chem.*, 2015, **80**, 661–665.
43 J. Hu, D. Zhang and F. W. Harris, *J. Org. Chem.*, 2005, **70**, 707–708.
44 X. Feng, J.-Y. Hu, C. Redshaw and T. Yamato, *Chem.–Eur. J.*, 2016, **22**, 11898–11916.
45 N. Ponugoti and V. Parthasarathy, *Chem.–Eur. J.*, 2022, **28**, e202103530.
46 F. Liu, X. Shen, Y. Wu, L. Bai, H. Zhao and X. Ba, *Tetrahedron Lett.*, 2016, **57**, 4157–4161.
47 D. Lungerich, D. Reger, H. Hölzel, R. Riedel, M. M. J. C. Martin, F. Hampel and N. Jux, *Angew. Chem.*, 2016, **128**, 5692–5696.
48 C. S. Frampton, K. S. Knight, N. Shankland and K. Shankland, *J. Mol. Struct.*, 2000, **520**, 29–32.
49 M. Tommasini, A. Lucotti, M. Alfè, A. Ciajolo and G. Zerbi, *Spectrochim. Acta, Part A*, 2016, **152**, 134–148.
50 A. Narita, I. A. Verzhbitskiy, W. Frederickx, K. S. Mali, S. Alkaersig Jensen, M. R. Hansen, M. Bonn, S. De Feyter, C. Casiraghi, X. Feng and K. Müllen, *ACS Nano*, 2014, **8**(11), 11622–11630.
51 R. Ulbricht, E. Hendry, J. Shan, T. F. Heinz and M. Bonn, *Rev. Mod. Phys.*, 2011, **83**, 543–586.
52 A. Tries, S. Osella, P. Zhang, F. Xu, C. Ramanan, M. Kläui, Y. Mai, D. Beljonne and H. I. Wang, *Nano Lett.*, 2020, **20**, 2993–3002.
53 G. Soavi, S. Dal Conte, C. Manzoni, D. Viola, A. Narita, Y. Hu, X. Feng, U. Hohenester, E. Molinari, D. Prezzi, K. Müllen and G. Cerullo, *Nat. Commun.*, 2016, **7**, 11010.
54 S. A. Jensen, R. Ulbricht, A. Narita, X. Feng, K. Müllen, T. Hertel, D. Turchinovich and M. Bonn, *Nano Lett.*, 2013, **13**, 5925–5930.
55 T. L. Cocker, D. Baillie, M. Buruma, L. V. Titova, R. D. Sydora, F. Marsiglio and F. A. Hegmann, *Phys. Rev. B*, 2017, **96**, 205439.